Available online at www.sciencedirect.com
SCIENCE DIRECT®
PERGAMON
International Journal of Heat and Mass Transfer 46 (2003) 1115–1137
International Journal of HEAT and MASS TRANSFER
www.elsevier.com/locate/ijhmt

Studies on turbulent momentum, heat and species transport during binary alloy solidification in a top-cooled rectangular cavity

S. Chakraborty [1], N. Chakraborty, P. Kumar, P. Dutta *

Department of Mechanical Engineering, Indian Institute of Science, Bangalore 560012, India

Received 3 August 2001; received in revised form 3 October 2002

Abstract

A two-dimensional transient fixed-grid enthalpy-based numerical method is developed to analyze the effects of turbulent transport during a binary alloy solidification process. Turbulence effects are introduced through standard k–ε equations, where coefficients are appropriately modified to account for phase-change. Microscopically-consistent estimates are made regarding temperature-solute coupling in a non-equilibrium solidification situation. The model is tested against laboratory experiments performed using an NH_4Cl–H_2O system in a rectangular cavity cooled and solidified from the top. Particular emphasis is laid on studying the interaction between Rayleigh–Benard type convection and directional solidification in the presence of turbulent transport. Numerical predictions are subsequently compared with experimental results regarding flow patterns, interface growth and evolution of the temperature field, and the agreement is found to be good.

1. Introduction

Significant effort has recently been devoted towards mathematical modeling of solidification processes, with the basic aim of enhancing both qualitative and quantitative understanding processes involving phase change. Further improvements in this area can eventually lead to more optimized process designs in applications such as metal casting, materials joining, semiconductor crystal growth and electronics cooling with phase change materials. Moreover, interactions between solidification and convection are of particular significance in developing deeper physical insights into various natural phenomena such as formation of icebergs and evolution of igneous rocks.

A typical solidifying system in many practical situations is the binary mixture. When a binary melt solidifies non-isothermally, the solidifying domain is characterized by separate solid and liquid regions, as well as a mushy region comprising of a matrix of solid, dendritic crystals with fluid-filled interstices. As solidification proceeds, the solute phase is rejected from solidifying dendrites in the mushy region. On a local scale, the solute is redistributed by diffusion transport. However, on a macroscopic scale, thermo-solutal convection currents carry the expelled solute further away from the site of rejection, and results in the so-called macrosegregation. Moreover, such interaction between double-diffusive convection and alloy solidification may be further complicated, in case the solidification is initiated by cooling a melt from the top. This is because the rate of heat and mass transfer during solidification may be influenced by Rayleigh–Benard type of cellular flow patterns formed below a continuously deforming interface, when the Rayleigh number exceeds a critical value for the onset of natural convection. In such a situation, flow conditions inside the melt may even be characterized by Rayleigh numbers

* Corresponding author. Tel.: +91-80-309-2589; fax: +91-80-360-0648.
E-mail address: pradip@mecheng.iisc.ernet.in (P. Dutta).
[1] Present address: Department of Mechanical Engineering, Indian Institute of Technology, Kharagpur 721302, India.

0017-9310/03/$ - see front matter
PII: S0017-9310(02)00402-7

Nomenclature

A	a coefficient in the Darcy source term
A_μ	a coefficient in Darcy source term
a_P, a_{P0}	coefficients in discretization equation
c	specific heat
C	species concentration
C_μ	proportionality constant in the formula of eddy viscosity
$C_{\varepsilon 1}$	modelling constant for production term in ε equation
$C_{\varepsilon 2}$	modelling constant for destruction term in ε equation
D	species mass diffusion coefficient
f_l	liquid fraction
f_μ	damping parameter for turbulent viscosity
F, G	constants in Darcy source term
F^{-1}	inverse of latent heat function
g_i	component of acceleration due to gravity in the ith direction
ΔH	latent heat content of a control volume
h	sensible enthalpy
h_l	height of liquid layer
k	turbulent kinetic energy
k_p	partition-coefficient
k_T	thermal conductivity
K	permeability
L	latent heat of fusion
p	pressure
R_t	turbulent Reynolds number
S_ϕ	source term for dependent variable ϕ
t	time
$\overline{T}$	mean temperature
T'	temperature fluctuation
$\overline{U}$, $\overline{V}$	mean velocity in x and y directions, respectively
$\overline{U}_i$	mean velocity in ith direction
u', v'	velocity fluctuation in x and y directions, respectively
u'_i	velocity fluctuation in ith direction
x_i	co-ordinate direction in ith direction
x, y	co-ordinate directions

Greek symbols

α	thermal diffusivity
α_t	eddy thermal diffusivity
β_T	thermal coefficient of volumetric expansion
β_S	solutal coefficient of volumetric expansion
ε	dissipation rate of kinetic energy
ϕ	general dependent variable
μ	dynamic viscosity
μ_t	turbulent viscosity
v	kinematic viscosity
σ_c, σ_k, σ_t, σ_ε	turbulent constants
ρ	density

Subscripts

c, cold	cold wall
h, hot	hot wall
l	liquid phase
L	liquidus
m	evaluated at melting point
max	maximum value
old	old iteration value
ref	reference state
i, 0	nominal or initial value

Superscript

n	level of iteration

exceeding a transitional value, leading to the onset of turbulence.

Numerous attempts, in general, have been made to understand the general transport mechanisms in binary alloy solidification processes, both theoretically and experimentally, as reviewed in [1]. A pioneering study for understanding the interaction between unidirectional solidification and convection that occurs when a melt is cooled from the top has been executed by a series of investigations undertaken by Kerr et al. [2–4] In their laboratory experiments, ice was frozen from a mixture of water and isopropanol. A continuum model was used to describe the partial differential equations governing heat and solute transport inside the domain. However, convective heat flux from the liquid region was calculated with a semiempirical formula appropriate for turbulent convection at high Rayleigh numbers, without resorting to detailed modeling for turbulence. Attempts towards bridging this gap have rarely been made in subsequent investigations, and hence, in the present paper, specific attention is paid to focus on significant issues of turbulent transport in the context of solidification processes of binary alloys.

A pioneering effort in incorporating the effects of turbulence in mathematical modeling of solidification during a Ti–6Al–4V alloy ingot casting was reported in Shyy et al. [5]. However, the treatment of turbulence was performed using a linear relation between eddy diffusivities and molecular values of viscosity and thermal conductivity. Shyy et al. [6] first used a modified turbulence model based on the standard k–ε two-equation closure to predict the phase change and convection–diffusion characteristics during titanium alloy ingot casting in an electron beam melting process. However,

the issues of species conservation did not feature in the physical process under investigation, and hence appropriate treatment of temperature-solute coupling, with associated microscale issues were not addressed. Subsequently, similar models were utilized to investigate various metallurgical processes, especially related to steel casting applications [7–9]. Recently Netto and Guthrie [10] employed a comprehensive k–ε model for heat transfer and fluid flow during solidification, in order to evaluate the performance of a novel delivery system for a single-belt steel casting process. However, simplifications in mushy zone modeling were made in the model by assuming that the latent heat is released between the liquidus and solidus temperatures in a uniform manner. Moreover, a steady state situation was assumed and natural convection effects were not included. Most significantly, issues of thermo-solutal coupling and microscopically consistent treatment of evolution of latent heat during the phase-change processes were not addressed.

The aim of the present work is to numerically analyze the effects of turbulent transport in a binary alloy solidification process, along with experimental validation. This is achieved by a macroscopic mathematical modeling that attempts to represent relevant microscopic issues in a metallurgically consistent manner. The model includes two-dimensional transient flow with coupled momentum, heat and species transfer. Natural convection effects are also included by introducing appropriate buoyant production terms. Turbulence effects are introduced through standard k–ε equations, in which coefficients are appropriately modified to account for phase-change. The release of latent heat between the liquidus and solidus temperatures is estimated from a temperature-solute coupling which includes the effect of non-equilibrium solidification and microscale transport. This results in microscopically consistent estimates of transport quantities in the regime of interest, by making use of appropriate governing equations for species distribution. To the best of our knowledge, modeling of turbulent transport during solidification of binary alloys, with due incorporation of the above features, is a matter yet to be addressed in the literature. In the present work, laboratory experiments are also performed using a metal-analog system, and simulation results are validated against the experimental observations.

2. Mathematical model

2.1. Description of the physical problem

The mathematical model is described with respect to a physical situation shown schematically in Fig. 1. A binary mixture (NH_4Cl–H_2O solution, in this case) is initially kept in a fully liquid state inside a two-dimensional rectangular cavity. Solidification is initiated by cooling the cavity from the top, while the side faces are kept insulated. The top and bottom wall temperatures, T_{cold} and T_{hot}, respectively, are obtained experimentally, as described subsequently in Section 4. The rectangular cavity is chosen to be of 160 mm width and 50 mm height. For the present top-cooled cavity with a height of 50 mm and with a nominal ΔT (i.e., $T_{\text{hot}} - T_{\text{cold}}$) of about 30 °C, the initial Rayleigh number is estimated to be of the order of 10^7, which is well within the turbulent regime. It can be noted here that the effective Rayleigh number (Ra) in the present study involves a solutal Rayleigh number (Ra_{S}), in addition to the existing thermal Rayleigh number (Ra_{T}), as given below:

$$Ra = Ra_{\text{T}} + Ra_{\text{S}}$$

i.e.,

$$Ra = \frac{g\beta_{\text{T}}[T_{\text{h}}(t) - T_{\text{c}}(t)]}{\alpha_{\text{l}} \nu_{\text{l}}} h_{\text{l}}^3(t) + \frac{g\beta_{\text{S}}[C_{\text{L}}(t) - C_i]}{\alpha_{\text{l}} D_{\text{l}}} h_{\text{l}}^3(t)$$

where $h_{\text{l}}(t)$ is the height of the liquid layer as a function of time. In the present case, with progress in solidification,

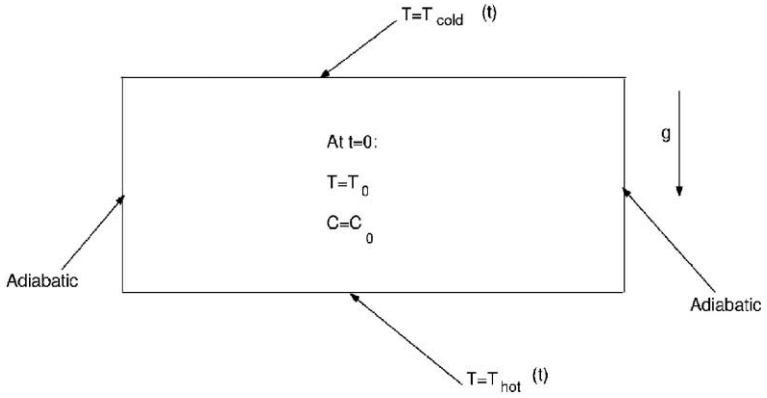

Fig. 1. A schematic diagram of the model problem.

the effective height of the liquid layer will continuously decrease, leading to a corresponding decrease of the Rayleigh number. Hence, the present system allows us to address the turbulent as well as laminar regimes of convection during directional solidification.

2.2. The conservation equations

The most important assumptions adopted in the mathematical model are listed below:

1. Solidification morphology is columnar dendritic.
2. Flow in the mushy region can be modeled as flow through a porous medium.
3. Thermo-physical properties can be evaluated by volume averaging of individual constituent properties of the mixture [11].
4. Evolution of latent heat in the solidification domain is influenced by microscale species transport.
5. Species redistribution during solidification is, in general, characterized by non-equilibrium effects [12].
6. Shrinkage effects during solidification are neglected.

Under the above assumptions, the governing conservation equations for the model problem can be written as follows.

2.2.1. Conservation of mass (continuity equation)

The single-phase continuity equation for an incompressible fluid is given by:

$$\frac{\partial \overline{U}_i}{\partial x_i} = 0, \quad \frac{\partial u_i'}{\partial x_i} = 0 \tag{1}$$

where the superscript (″) represents the fluctuating component of a scalar variable.

2.2.2. Conservation of linear momentum

The equivalent single-phase linear momentum conservation equation for the i'th direction is given by ($i = 1, 2$):

$$\begin{aligned}\frac{\partial(\rho\overline{U}_i)}{\partial t} + \frac{\partial(\rho\overline{U}_i\overline{U}_j)}{\partial x_j} = &-\frac{\partial p}{\partial x_i} + \frac{\partial}{\partial x_j}\left(\mu\frac{\partial \overline{U}_i}{\partial x_j}\right) \\ &- \frac{\partial(\rho\overline{u_i'u_j'})}{\partial x_j} + \rho g_i[\beta_T(\overline{T} - T_{ref}) \\ &+ \beta_S(\overline{C}_l - C_{ref})] - A\overline{U}_i\end{aligned} \tag{2}$$

where g_i is the component of acceleration due to gravity in the ith direction, T_{ref} and C_{ref} are reference values of temperature and concentration, respectively. The source term $A\overline{U}_i$ in Eq. (2) originates from the consideration that the morphology of the phase change domain can be treated as an equivalent porous medium that offers a frictional resistance towards fluid flow in that region, the modelling of which is detailed in Section 2.3. The term $-\partial/\partial x_j(\rho\overline{u_i'u_j'})$ is called Reynolds stress term, the modeling of which is detailed in Section 2.4.

2.2.3. Conservation of energy

The single-phase energy equation for turbulent flow is given by:

$$\begin{aligned}\frac{\partial(\rho\overline{T})}{\partial t} + \frac{\partial(\rho\overline{U}_i\overline{T})}{\partial x_i} = &\frac{\partial}{\partial x_i}\left(\{f_l k_{T_l}/c_l + (1 - f_l)k_{T_s}/c_s\}\frac{\partial \overline{T}}{\partial x_i}\right) \\ &- \frac{1}{c}\frac{\partial(\rho\Delta H)}{\partial t} - \frac{1}{c}\frac{\partial}{\partial x_i}\left(\overline{U}_i\Delta H\right) \\ &- \frac{\partial(\rho\overline{u_i'T'})}{\partial x_i}\end{aligned} \tag{3}$$

where c is the specific heat, k_T is the thermal conductivity, and ΔH is the latent enthalpy content of the control volume under consideration.

2.2.4. Species conservation

It is well-known that binary systems, which exhibit limited solid-solubility, typically exhibit non-equilibrium solidification, since dendrites are not chemically saturated due to the slow nature of solid-state diffusion [13]. Thus, equilibrium freezing assumptions may provide inaccurate predictions of local solute segregation between liquid and solid phases and of phase volume fraction [14]. Hence, in the present model, we address a situation that considers non-equilibrium species redistribution on solidification, resulting in a columnar dendritic growth with a distinct microstructure [12]. The key point is that the solute concentration within the bulk liquid may be uniform over microscopic distances but may have a non-uniform profile in the solid. With an additional assumption of no local remelting, the final form of species conservation equation becomes:

$$\begin{aligned}\frac{\partial(\rho\overline{C}_l)}{\partial t} + \frac{\partial(\rho\overline{U}_i\overline{C}_l)}{\partial x_i} = &\frac{\partial}{\partial x_i}\left(\rho_l f_l D_l\frac{\partial \overline{C}_l}{\partial x_i}\right) - \frac{\partial(\rho\overline{u_i'C_l'})}{\partial x_i} \\ &+ \frac{\partial}{\partial t}(\rho f_s\overline{C}_l) - k_p\overline{C}_l\frac{\partial}{\partial t}(\rho f_s)\end{aligned} \tag{4}$$

where k_p is the partition-coefficient.

2.2.5. Governing equations for k and ε

The governing equations for k and ε in the present context can be written as:

$$\begin{aligned}\frac{\partial(\rho k)}{\partial t} + \overline{U}_i\frac{\partial(\rho k)}{\partial x_i} = &\frac{\partial}{\partial x_i}\left[\left(\mu + \frac{\mu_t}{\sigma_k}\right)\frac{\partial k}{\partial x_i}\right] + \left[\mu_t\left(\frac{\partial \overline{U}_i}{\partial x_j}\right.\right. \\ &\left.\left. + \frac{\partial \overline{U}_j}{\partial x_i}\right)\frac{\partial \overline{U}_i}{\partial x_j}\frac{\varepsilon}{k} - g\beta_T\frac{\mu_t}{\sigma_t}\frac{\partial \overline{T}}{\partial y}\frac{\varepsilon}{k}\right. \\ &\left. - g\beta_S\frac{\mu_t}{\sigma_c}\frac{\partial \overline{C}_l}{\partial y}\right] - \rho\varepsilon\end{aligned} \tag{5}$$

$$\frac{\partial(\rho\varepsilon)}{\partial t}+\overline{U}_i\frac{\partial(\rho\varepsilon)}{\partial x_i}=\frac{\partial}{\partial x_i}\left[\left(\mu+\frac{\mu_t}{\sigma_\varepsilon}\right)\frac{\partial\varepsilon}{\partial x_i}\right]+\frac{C_{\varepsilon1}\varepsilon}{k}\left[\mu_t\left(\frac{\partial\overline{U}_i}{\partial x_j}+\frac{\partial\overline{U}_j}{\partial x_i}\right)\frac{\partial\overline{U}_i}{\partial x_j}\frac{\varepsilon}{k}-g\beta_T\frac{\mu_t}{\sigma_t}\frac{\partial\overline{T}}{\partial y}\frac{\varepsilon}{k}-g\beta_S\frac{\mu_t}{\sigma_c}\frac{\partial\overline{C}_l}{\partial y}\right]-\rho C_{\varepsilon2}\frac{\varepsilon^2}{k} \quad (6)$$

The values of various turbulence constants appearing in the above equations are as follows:

$$C_\mu=0.9,\quad \sigma_t=0.9,\quad \sigma_c=0.9,\quad \sigma_k=1.0,$$
$$\sigma_\varepsilon=1.3,\quad C_{\varepsilon1}=1.44,\quad C_{\varepsilon2}=1.92$$

It can be observed from the above that the conservation of mass, momentum, energy and species, as well as closure equations involving k and ε can be represented in a general convection–diffusion conservative form as [15]:

$$\frac{\partial(\rho\phi)}{\partial t}+\frac{\partial}{\partial x_i}(\rho u_i\phi)=\frac{\partial}{\partial x_i}\left(\Gamma_{\text{eff}}\frac{\partial\phi}{\partial x_i}\right)+S_\phi \quad (7)$$

where ϕ is the general scalar variable; x_i is the coordinate in the Cartesian system; u_i is the component of mean velocity in direction x_i; Γ_{eff} is the effective diffusion coefficient for the variable ϕ; S_ϕ is the source term for the dependent variable ϕ. The values of ϕ, Γ_{eff}, and S_ϕ for various conservation equations are given in Table 1.

Since mixture properties may vary over the two-phase region, non-dimensionalization of the governing equations (i.e., normalization with respect to some constant values of material properties) may not be very appropriate in this case, as far as solution of the governing equations is concerned. Therefore, we have preferred a dimensional scheme for solution of the coupled set of conservation equations. However, it must be recognized that one of the primary objectives of the present work is to investigate a general mode of interaction between momentum and heat transfer during the directional solidification process. Accordingly, a dimensionless scheme has been employed for post-processing of the results from the present investigation, typically depicting a relationship between significant dimensionless parameters such as the effective Rayleigh number (Ra) and the Nusselt number (Nu) based on heat flux at the liquidus interface.

Table 1
Table of diffusion coefficients and source terms for various conservation equations

Equation	ϕ	Γ_{eff}	S_ϕ
Continuity	1	0	0
x momentum	$\overline{U}$	$\mu+\mu_t$	$\frac{\partial}{\partial x_j}\left(\Gamma_{\text{eff}}\frac{\partial\overline{U}}{\partial x_j}\right)-A\overline{U}-\frac{\partial p}{\partial x}$
y momentum	$\overline{V}$	$\mu+\mu_t$	$\frac{\partial}{\partial x_j}\left(\Gamma_{\text{eff}}\frac{\partial\overline{V}}{\partial x_j}\right)-A\overline{V}-\frac{\partial p}{\partial y}+\rho g\left[\beta_T(\overline{T}-T_{\text{ref}})+\beta_C(\overline{C}_l-C_{\text{ref}})\right]$
Energy	$\overline{T}$	$f_l\frac{k_{T_l}}{c_l}+(1-f_l)\frac{k_{T_s}}{c_s}+\frac{\mu_t}{\sigma_t}$	$-\frac{1}{c}\left[\frac{\partial}{\partial t}(\rho f_l\Delta H)+\frac{\partial}{\partial x_j}(\rho u_j\Delta H)\right]$
Species	$\overline{C}_l$	$\rho f_l D_l+\frac{\mu_t}{\sigma_c}$	$\frac{\partial}{\partial t}\left[\rho f_s\overline{C}_l\right]-k_p\overline{C}_l\frac{\partial}{\partial t}(\rho f_s)$
Turbulent kinetic energy	k	$\frac{\mu_t}{\sigma_k}+\mu$	$\mu_t\left(\frac{\partial\overline{U}_i}{\partial x_j}+\frac{\partial\overline{U}_j}{\partial x_i}\right)\frac{\partial\overline{U}_i}{\partial x_j}-g\beta_T\frac{\mu_t}{\sigma_t}\frac{\partial\overline{T}}{\partial y}-g\beta_C\frac{\mu_t}{\sigma_c}\frac{\partial\overline{C}_l}{\partial y}-\rho\varepsilon$
Dissipation rate of turbulent kinetic energy	ε	$\frac{\mu_t}{\sigma_\varepsilon}+\mu$	$\left[\mu_t\left(\frac{\partial\overline{U}_i}{\partial x_j}+\frac{\partial\overline{U}_j}{\partial x_i}\right)\frac{\partial\overline{U}_i}{\partial x_j}-g\beta_T\frac{\mu_t}{\sigma_t}\frac{\partial\overline{T}}{\partial y}-g\beta_C\frac{\mu_t}{\sigma_c}\frac{\partial\overline{C}_l}{\partial y}\right]\frac{C_{\varepsilon1}\varepsilon}{k}-\rho\frac{C_{\varepsilon2}\varepsilon^2}{k}$

2.3. Flow modelling in the mushy zone

In the present model, it is assumed that the phase-change domain is a saturated porous medium that offers frictional resistance to fluid flow in that region. Since the framework of this model is fairly general, any appropriate porous-medium model can be chosen to describe the flow in the region undergoing a phase-change, in accordance with the morphology of the phase-change domain. It can be noted here that the aim of the present study is not to assess the appropriateness of several porous medium models available in contemporary literature. Hence, for simplicity, we use a modified Darcy's model [16] which is described subsequently. The above model of viscous flow through a porous medium (assuming an isotropic permeability) leads to the following source term in the momentum equation:

$$-A\bar{u} = -\frac{\mu_l \rho \bar{u}}{K \rho_l} \tag{8a}$$

and

$$-A\bar{v} = -\frac{\mu_l \rho \bar{v}}{K \rho_l} \tag{8b}$$

where K is the permeability. For appropriate modeling of the above term, K has to be properly prescribed as a function of liquid fraction, f_l. For that purpose, the Carman–Kozeny relation [14] is used within the range of validity: $0 < f_l < 0.5$; i.e.,

$$K = K_0 \frac{f_l^3}{(1-f_l)^2} \tag{9}$$

where K_0 is the porosity constant. However, due to inaccuracy of this equation for $f_l > 0.5$, a hybrid model is used for that region [16], as given by:

$$\mu_l = \mu_l^0 \left\{ \frac{A_\mu}{A_\mu - F(1-f_l)} \right\}^2 \tag{10}$$

and

$$K = GK_0 \left[\frac{f_l^3}{(1-f_l)^2} \right], \quad A_\mu = 0.4 \tag{11}$$

Here, F and G are obtained from the theory of rheology of suspensions. Their role is to reduce the effects of excessive damping action of the Darcy-force, and are expressed as:

$$F = 0.5 - \frac{1}{\pi} \arctan[100(f_l^{cr} - f_l)] \tag{12}$$

$$G = 0.5 + \frac{1}{\pi} \arctan[100(f_l^{cr} - f_l)]^{-4}, \quad \text{where } f_l^{cr} = 0.5 \tag{13}$$

In the above equations, f_l^{cr} can be considered as a critical liquid fraction upto which the Carman–Kozeny equation remains valid.

2.4. Modeling of turbulence parameters

2.4.1. Modelling of Reynolds stress terms ($-\rho\overline{u_i' u_j'}$)

In the enthalpy-porosity formulation, because of modification of usual Navier–Stokes equations made by the porous medium source terms, the velocity field in the mushy zone does not yield information to distinguish dendrites from the melt precisely. There have been only a few attempts of turbulence modeling in this context. A recent attempt has been made by Masuka and Takatsu [17] with regard to turbulence modeling in flow through porous medium. The above model has subsequently been discussed by Netto and Guthrie [10], and its use in the context of solidification modeling has been debated. However, from physical considerations, the flow in the mushy region is expected to be laminar. Accordingly, in the present work, although the k–ε-model is applied to the whole domain, particular considerations are made to satisfy the following two limiting conditions at the phase boundaries:

1. The model should reduce the eddy viscosity, turbulent Prandtl number, and Schmidt numbers to their respective molecular values along the solidus front.
2. The model should merge with single-phase turbulence closure equations in pure liquid region in a smooth manner.

In the present analysis, we model the Reynolds stress terms appearing in Eq. (2) by assuming a turbulent viscosity of the form:

$$-\rho\overline{u_i' u_j'} = \mu_t \left(\frac{\partial \overline{U}_i}{\partial x_j} + \frac{\partial \overline{U}_j}{\partial x_i} \right) - \frac{2}{3}\delta_{ij} k \tag{14}$$

where

$$\mu_t = f_\mu C_\mu \rho k^2 / \varepsilon \tag{14a}$$

In Eq. (14a), C_μ is a constant, whose value has been experimentally determined from shear flow experiments. It is reported that C_μ varies from 0.08 to 0.09 [18]. The function f_μ can be described as a function of liquid fraction and turbulent Reynolds number ($R_T = (\rho k^2/\mu\varepsilon)$) as [6]:

$$f_\mu = \sqrt{f_l} \exp\left[\frac{-3.4}{\left(1 + \frac{R_T}{50}\right)^2} \right] \tag{15}$$

The above exponential form of the function provides a smooth transition of turbulent viscosity from a deactivated state in the fully solid region to a completely activated state in the fully liquid region. The exponential

function also ensures continuity of the turbulent viscosity across the logarithmic layer in the vicinity of the solid interfaces.

2.4.2. Modelling of turbulent heat fluxes ($-\rho\overline{u_i'T'}$)

Following the same analogy as the Reynolds stresses, the turbulent heat fluxes (Reynolds heat fluxes) appearing in Eq. (3) can be written as:

$$-\rho\overline{u_i'T'} = \rho\alpha_t\frac{\partial\overline{T}}{\partial x_i} \tag{16}$$

where α_t the eddy thermal diffusivity. From the analogy of laminar flow, α_t can be expressed as:

$$\alpha_t = \frac{\mu_t}{\rho\sigma_t} \tag{16a}$$

where σ_t turbulent Prandtl number. It has been proposed that σ_t varies from 0.8 to 0.9. In the present work, we take $\sigma_t = 0.9$.

2.4.3. Modelling of turbulent mass fluxes ($-\rho\overline{u'C_l'}$)

Following the same analogy as the Reynolds stresses, the turbulent mass fluxes (Reynolds mass fluxes) appearing in Eq. (4) can be written as:

$$-\rho\overline{u_i'C_l'} = \rho D_t\frac{\partial\overline{C_l}}{\partial x_i} \tag{17}$$

where D_t the eddy mass diffusivity. From the analogy of laminar flow, D_t can be expressed as:

$$D_t = \frac{\mu_t}{\rho\sigma_c} \tag{17a}$$

where σ_c is the turbulent Schmidt number. In the present work, we take $\sigma_c = 0.9$.

2.5. Initial and boundary conditions

The initial conditions appropriate to the physical problem are:

At $t = 0$, $T = T_0$, $C_l = C_0$, $f_l = 1$.

The following boundary conditions are adopted for solution of conservation equations:

1. No-slip conditions at the walls, i.e., $u = v = 0$.
2. Specified temperature at the top ($T = T_{cold}$) and bottom ($T = T_{hot}$) walls. In the present work, the top and bottom temperatures are specified using experimental measurements as described in Section 4).
3. Insulated side walls, i.e., $\partial T/\partial x = 0$.
4. Zero solute gradient at the walls, i.e., $\partial C_l/\partial y = 0$ at top and bottom walls, and $\partial C_l/\partial x = 0$ at the side walls.
5. Zero value of k and ε at the solid walls.

It can be noted that, since we follow a fixed-grid single-domain enthalpy-porosity approach [19] for solution of conservation equations, the interface locations come out as direct outcome of the solution procedure itself, and thus need not be tracked separately. Also, prescription of boundary conditions at the interface locations is not required.

3. Numerical analysis

3.1. The numerical scheme

The coupled conservation equations are solved using a pressure-based finite volume method according to the SIMPLER algorithm [15]. The algorithm is appropriately modified to account for turbulent transport in the presence of continuously evolving solidification interfaces. The broad steps followed for numerical solution of the governing equations are as follows:

Step 1: Guess the velocity field.
Step 2: Use the initial and boundary conditions to solve for the pressure equation, pressure correction equation, and momentum equations as per SIMPLER algorithm, in order to obtain an updated velocity and pressure field.
Step 3: Solve for energy and species conservation equations (details of discretization of convection–diffusion terms are mentioned in Appendix A).
Step 4: Update nodal enthalpy values consistent with microscopic considerations.
Step 5: Obtain a value of C_μ from updated liquid fraction, and accordingly update the value of μ_t.
Step 6: Using updated values of μ_t, solve for k and ε equations.
Step 7: Check for convergence. In case convergence criteria are fulfilled, proceed to the next time-step. Otherwise, go back to step 2 and iterate until convergence is achieved within the present time-step.

From the description of the above algorithm, it is evident that microscopically consistent updating of f_l and C_μ plays a major role towards successful implementation of the present scheme, apart from the solution of the conservation equations. Further details of these updating schemes are outlined in Appendices B and C.

3.2. Choice of grid-size, time-step and convergence criteria

A comprehensive grid-independence study is undertaken to determine the appropriate spatial discretization, temporal discretization and iteration convergence criteria to be used. The quantities examined in this study

are the maximum magnitudes of the various scalar variables (i.e. horizontal and vertical velocity components, temperature, solute concentration in the liquid, turbulent kinetic energy, and dissipation rate of turbulent kinetic energy), the interface location and its growth rate. As an outcome of this study, we have taken a 100×100 non-uniform grid as our final simulation matrix, with very fine grids along the y-direction near the top wall ($\sim$0.05 mm). Also, we have adopted a gradually increasing time step, starting from an initial value of 0.1 s to a final value of 1 s for the later stages. Selection of such gridding and time step is primarily meant to capture the initial transients, as the solidification begins. Also, small time-steps ensure that the predictions regarding the interface growth rates are accurate enough. However, it is found that, a finer grid system and time step size is unable to alter the results appreciably. A summary of the grid-independence study, involving the evaluation of solution fields of a test matrix of simulations with four different mesh spacing and four different time-step sizes is presented in Table 2.

Convergence in inner iterations is declared only when the following conditions are simultaneously satisfied:

1. $|(\phi - \phi_{\text{old}})/\phi_{\max}| \leqslant 10^{-4}$, where ϕ stands for each variable u, v, T and C_l, k, ε at a grid point at the current iteration level, ϕ_{old} represents the corresponding value at the previous iteration level, and $\phi_{\max}$ is the maximum value of the variable at the iteration level in the entire domain.
2. Absolute values of the energy balance are within 0.1% of the total stored energy within the computational domain.

4. Experimental arrangement

The experimental setup for the present study consists of a rectangular cavity with inner dimensions as 160 mm (width) $\times$ 50 mm (height) $\times$ 90 mm (depth) (refer to Fig. 2a), filled with an NH_4Cl–H_2O solution of a nominal composition of 15% by weight of NH_4Cl. The plane of visualization is chosen to be the longitudinal plane (160 mm $\times$ 50 mm) midway along the depth of the cavity. The boundary conditions are so chosen that fluid flow and interface growth are essentially two-dimensional in this plane. The side walls of the tank are made of Plexiglas, which has a low thermal conductivity. The bottom wall consists of a copper block of 25 mm thickness, which ensures a uniform bottom surface temperature. The bottom plate is insulated underneath with a 10 mm thick sheet of cork. Heat leakage from the top face above the heat exchanger is minimized by using a Styrofoam insulation of 25 mm thickness. The side faces of the cavity are effectively insulated by placing the test cavity in a larger Plexiglas tank, with a partially evacuated air gap of 25 mm thickness maintained between the inner and outer surfaces of the insulated walls. All cold lines in the circuit are insulated with polyurethene tubing. The dimensions of the cavity and the boundary conditions result in a predominantly two-

Table 2
Effect of grid size and time-step size on numerical results

Grid Size	$\lvert u_{\max}\rvert \times 10^2$ (m/s)	$\lvert v_{\max}\rvert \times 10^2$ (m/s)	$T_{\max}$ (°C)	$C_{l,\max}$ (wt.% NH_4Cl)
Panel (a)				
120×120	0.86711 (65,35) 0.011%	0.74333 (72,34) 0.041%	−7.3200 (80, 0.25) 0.010%	15.8350 (80, 38.2) 0.007%
100×100	**0.86710 (65,35) 0.012%**	**0.74320 (72, 34) 0.043%**	**−7.3124 (80,0.25) 0.011%**	**15.8342 (80,38.25) 0.008%**
80×80	0.85412 (60, 32) 1.508%	0.69143 (78, 32) 6.565	−8.6011 (80, 0.4167) 17.341%	15.3667 (84, 36.5) 0.443%
60×60	0.8445 (58, 28) 8.667%	0.6001 (70, 28) 18.122%	−8.5667 (80, 0.5) 21.468%	15.0001 (80, 35) 1.035%
Minimum time step size Δt (s)	$\lvert u_{\max}\rvert \times 10^2$ (m/s)	$\lvert v_{\max}\rvert \times 10^2$ (m/s)	$T_{\max}$ (°C)	$C_{l,\max}$ (wt.% NH_4Cl)
Panel (b)				
0.05	0.86711 (65,35) 0.011%	0.74322 (72,34) 0.043%	−7.3122 (80, 0.25) 0.010%	15.8344 (80, 38.25) 0.007%
0.1	**0.86710 (65,35) 0.012%**	**0.74320 (72, 34) 0.043%**	**−7.3124 (80,0.25) 0.011%**	**15.8342 (80,38.25) 0.008%**
0.5	0.86709 (64, 35) 0.015%	0.74319 (70, 34) 0.898%	−7.3001 (80, 0.25) 0.028%	15.8295 (78, 38.2) 0.087%
0.75	0.85246 (70, 28) 4.787%	0.70021 (70, 28) 4.545%	−7.6125 (80,0.25) 0.079%	15.9776 (78, 38.2) 0.344%

Panel (a): Effect of grid size on results: Numbers in the bracket represent locations (mm, mm) in the cavity (with respect to the bottom left corner), where the quoted values occur. The percentages quoted represent relative errors corresponding to the above quoted values. The time-step size is taken as $\Delta t = 0.1$ s, for all cases. All results correspond to $t = 5000$ s.
Panel (b): Effect of time-step size on results: Numbers in the bracket represent locations (mm, mm) in the cavity (with respect to the bottom left corner), where the quoted values occur. The percentages quoted represent relative errors corresponding to the above quoted values. The grid size is taken as 100×100, for all cases. All results correspond to $t = 5000$ s.

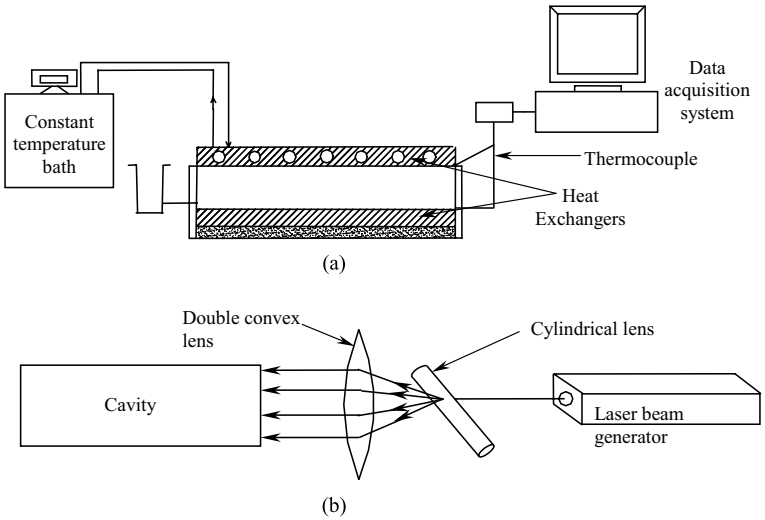

Fig. 2. Schematic diagram of the experimental arrangement (a) overall experimental setup, (b) lighting arrangement for flow visualization.

dimensional solidification behaviour in the plane of visualization. The top surface of the cavity comprises of a cooling plate made of oxygen-free electrolytic copper. The coolant used is pure ethanol that is cooled in a Julabo-FP40 programmable microprocessor-controlled constant-temperature bath. The bath capacity is 12 l of ethyl alcohol under a pressure head of 290 mb. The coolant's path through the heat exchanger has been designed to ensure an efficient heat extraction. The pumping rate of the circulator can be upto 20 litres per minute and the fluctuations of the controlled temperatures lie within ± 0.01 °C.

The experiment is initiated by switching on the bath, which is initially maintained at the same temperature as that of the working fluid inside the test cavity. After the bath is switched on, the top surface temperature of the cavity decreases rapidly, and then asymptotically approaches a near steady-state value, as shown in Fig. 3.

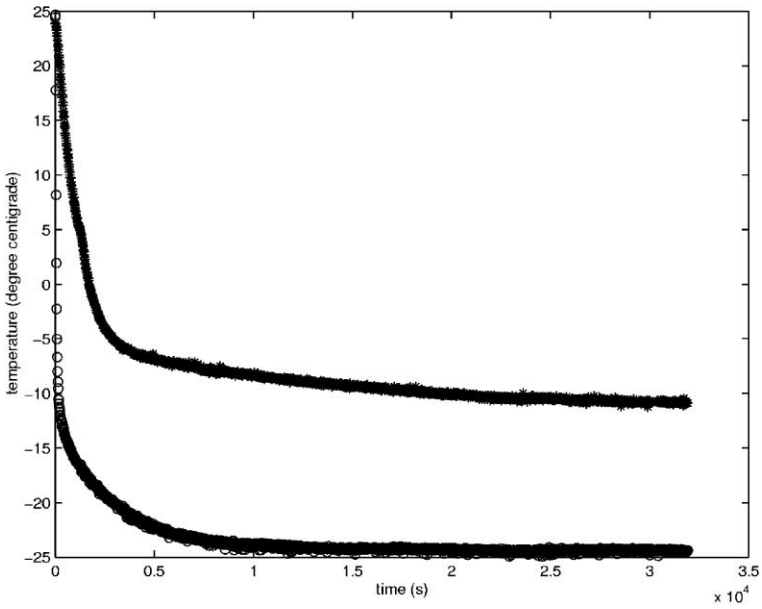

Fig. 3. Variation of temperature with time at the top and bottom boundaries.

Typically, it takes about two hours for both the wall temperatures (top and bottom) to attain near steady-state values.

The thermal evolution of the experiment is monitored using a Keithley DASTC 16 channel thermocouple card, with copper-constantan T-type 30 gage Teflon-coated copper-constantan thermocouples (manufactured by TC Ltd., UK) as temperature sensors. They are calibrated against a platinum resistance thermometer possessing an accuracy of ± 0.01 °C. The uncertainty in temperature measurement with the thermocouples is ± 0.2 °C. The data acquisition system consists of a Pentium-based personal computer, which records the temperature variation with time. Seven thermocouples are inserted into the cavity at various locations in a vertical plane and are supported on a wire-frame. The other nine thermocouples are routed through the heat exchanger channels and the pathways, and located in the vicinity of the top and bottom walls. Holes of 0.7 mm diameter are drilled at different locations staggered on the top as well as the bottom plate, through which thermocouples are inserted and are sealed with a high-conductivity thermal paste. The variation of the top and bottom wall temperatures with time, as obtained under experimental conditions, is shown in Fig. 3. Since these wall temperatures are also used as boundary conditions for the numerical simulation, extreme care is exercised to ensure the consistency of the measured temperatures. This is done by executing numerous experimental runs, (typically 16 in number) and thereby assessing the repeatability of the temperature measurements by the thermocouples.

During the experiments, we observe the growth of the solid layer through the transparent front wall of the cavity. The interface is photographed and zoomed in to identify its precise location at any given time from the scales (graduated in millimetres) attached to the outer surfaces of the test-piece. The evolution of the interface is monitored by direct photography using diffused lighting. However, such visualization arrangements are not adequate for recording the cellular convective flow pattern accompanying the solidification process. Accordingly, the fluid flow is visualized by employing a sheet of red-coloured helium-neon laser light having a power of 45 mW. The laser light is scattered by neutrally buoyant hollow glass spheres (dia. ranging from 40–60 μm) seeded in the cavity fluid. It is ensured that the solution containing neutrally buoyant glass spheres has the same concentration as that of the test-fluid. However, independent runs without introducing glass spheres have also been conducted to confirm that there is no additional effect on solidification caused by the introduction of glass spheres. Conglomeration between the glass particles is prevented by introducing a small amount of soap solution into the cavity. Photographs are taken using a normal 35 mm SLR camera. The above arrangement enables us to conveniently visualize the overall flow-field characterized by the presence of convecting cells in conjunction with the evolving solidification interface, depicting the interaction between Rayleigh–Benard convection and directional solidification. The temperature measurement and flow visualization experiments are conducted separately so as not to interfere with each other. The flow visualization arrangements are sketched in Fig. 2b.

5. Results and discussion

Once cooling is initiated from the top, natural convection begins inside the cavity. The convection is similar to classical Rayleigh–Benard convection, resulting in typical cellular flow patterns. The cellular convection enhances the heat transfer in the liquid layer, which is being cooled as a result of heat exchange taking place at the top wall. Once the liquid in the vicinity of the top wall attains a temperature lower than the solidus temperature, nucleation occurs which subsequently leads to the formation of a stable solid front attached to the top wall. However, there is a distinct difference in the interface patterns that are observed in the present case, as compared to the ones in the presence of laminar Rayleigh–Benard type convection [19]. In laminar Rayleigh–Benard convection, the convective cells are usually characterized by zones of up-flow and down-flow motions of warm and cold fluid streams, respectively, leading to a wavy interface growth [19]. Solidification rate is retarded near the zones where warm fluid streams rise towards the interface. On the other hand, solidification rate is enhanced at locations characterized by descending cold fluid streams. The above phenomenon results in a formation of crests and troughs at the interface in such situations [19]. However, in the present case, convection is characterized by turbulent transport that results in an enhanced mixing inside the fluid. Although the mean flow is still characterized by large-scale cellular motion, the enhanced thermal diffusivity in this case does not allow the interface to become wavy. Moreover, the thickness of the mushy zone formed below the solidified phase is also perceptibly smaller than in case of a laminar flow [19]. This is because of the fact that turbulent fluid motion induces high thermal and solutal gradients just below the interface, thus bringing the solidus and liquidus fronts closer to each other. This effectively ''washes out'' the mushy zone, resulting in a situation almost similar to that of freezing of a single-component system.

The evolution of fluid flow along with the liquidus interface is depicted in Figs. 4–11, which show the numerically obtained streamlines and interface locations at different instances of time, until the flow dies down. The thermophysical properties for numerical simulation are

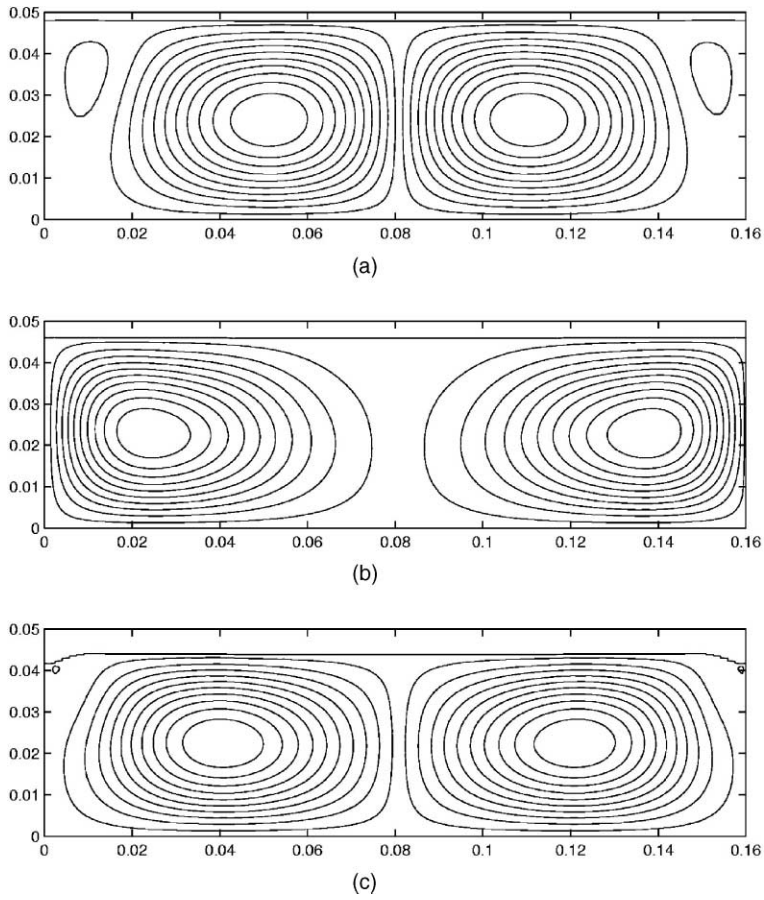

Fig. 4. Evolution of flow with time, as obtained from numerical simulation at (a) $t = 1200$ s, (b) $t = 1800$ s and (c) $t = 2500$ s. All dimensions are in m.

taken from Voller et al. [12]. A trend of continuously evolving flow-field and interface can be seen from the above figures, which is supported by experimental observations as well. From the above figures, it can be clearly seen that the flow-field is initially characterized by two major circulating loops. Subsequently (at approximately $t = 3600$ s), the loops tend to break down into smaller cells approaching towards the side-walls of the cavity. Eventually, at approximately $t = 4000$ s, four major loops can be observed; specifically two big loops in the central region accompanied by two small loops near the side faces. At about $t = 5000$ s, the big loops at the central portion become unstable, and subsequently they become envelopes of two distinct counter-rotating cells (at approximately $t = 6000$ s). At about $t = 7200$ s, the central cells stabilize again. However, transitions in the mode of convection continuously tend to make the configurations of these cells fluctuate, as the height of the liquid layer continuously diminishes. In the process, the cells formed in the vicinity of the side walls get continuously stretched, as time progresses. The aspect ratios (length: width) of these cells increase progressively, and those for the central cells decrease continuously. At about $t = 16000$ s, the four cells eventually break down into five cells of different sizes. These cells subsequently tend to stretch and fold, in order to be accommodated in a continuously thinning liquid layer. At about $t = 39500$ s, the two cells at the middle of the domain suddenly disappear, and the other two cells progressively move towards the corner of the cavity, until the fluid flow eventually dies down at about $t = 42000$ s. At the corresponding liquid layer height, the thermo-solutal buoyancy forces become too weak to maintain natural convection against dissipative viscous forces.

In order to have a clear visualization of the cellular flow patterns, experimental photographs depicted in Fig. 12 can be referred to. Fig. 12a shows a zoomed portion in the middle plane of the cavity. It is apparent that the experimentally obtained flow-pattern shown in Fig. 12a resembles a corresponding numerical simulation shown in Fig. 7a, where two central counter-rotating vortices

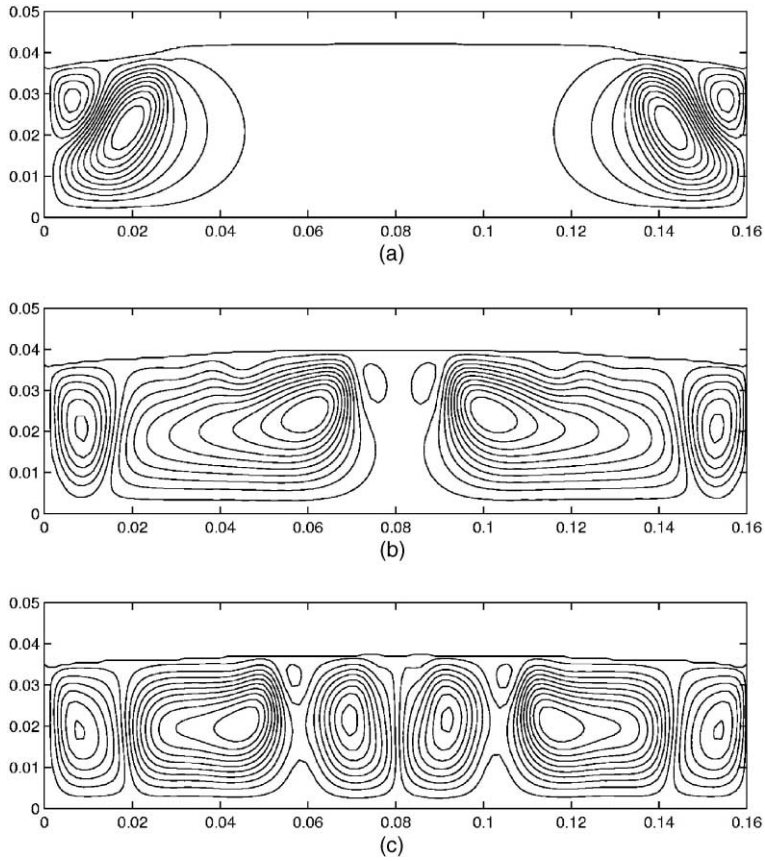

Fig. 5. Evolution of flow with time, as obtained from numerical simulation at (a) $t = 3600$ s, (b) $t = 4000$ s and (c) $t = 5000$ s. All dimensions are in m.

can be observed. Fig. 12b depicts a zoomed portion near the right corner of the cavity, where a small vortex near the wall is accompanied by a larger vortex stretching towards the center of the cavity. The above trend compares well with the corresponding numerical simulation shown in Fig. 7b. The evolution of the solidifying interface is also captured during the experiments, as shown in Fig. 13. For qualitative and quantitative evaluation of the interface growth, the overall evolution of the visualization experiment is summarized in Fig. 14, where the experimental results are also compared with the corresponding numerical predictions. The average thickness (taken across the entire horizontal distance in the plane of visualization) of the solid layer and mushy layer are plotted against time in Fig. 14. From Fig. 14, we observe that the average thickness of the solid and the mush with time are predicted with reasonable accuracy by the present model. Nucleation starts at about $t = 900$ s after initiation of the experiment. The nucleation is typically characterized by the formation of tiny crystals on the top wall, capable of further growth. In about 1250 s, a continuous solid layer of about 2 mm in thickness can be observed at the top. Thereafter, the interface grows in a stable fashion, leading to a thickening of the solid layer, and consequently, a thinning of the liquid layer. Regarding the growth of the mushy zone, an interesting feature is observed. The mushy zone initially grows in a stable fashion till about $t = 7500$ s, though the growth rate is much slower than that of the solid interface. Further, the relative size of the mushy zone with respect to that of the total height of solid and mushy layers seems to be smaller than that produced in the presence of a laminar Rayleigh–Benard convection [19]. After about $t = 10\,000$ s, the mushy layer height eventually starts decreasing, and almost goes to zero after about $t = 25\,000$ s. The entire phenomenon can be explained as follows. At initial periods of turbulence, the mushy zone cannot grow at a fast pace, because of enhanced turbulent mixing, as explained earlier. The mushy layer thickness increases gradually in the beginning, but the growth rate decreases with progress in solidification. As solidification progresses, NH_4Cl is being constantly released in the liquid, thereby increasing its concentration in the bulk liquid, bringing it closer

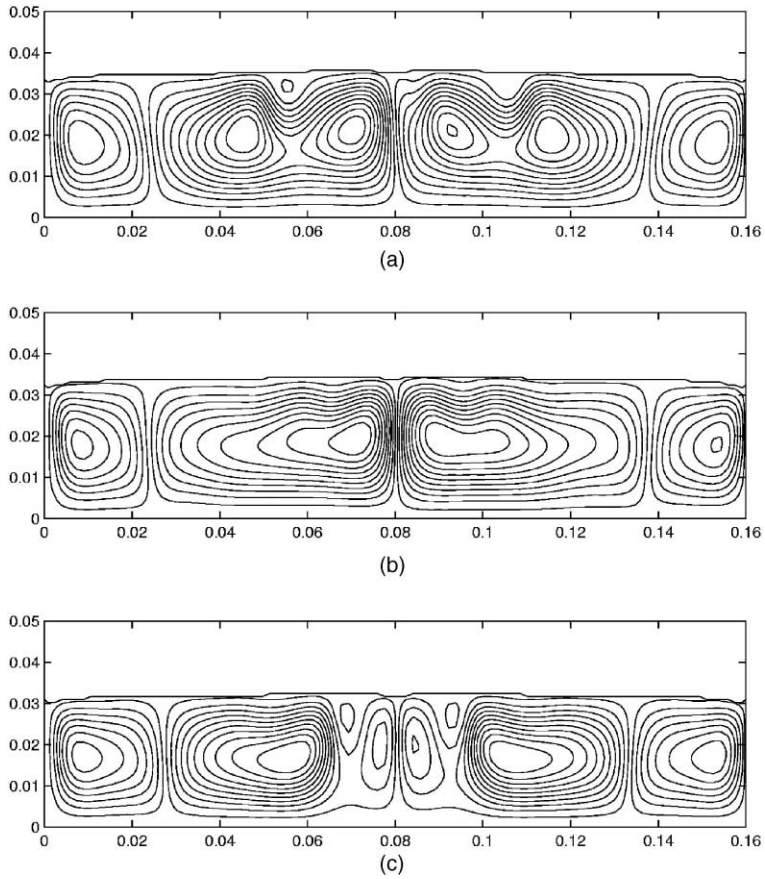

Fig. 6. Evolution of flow with time, as obtained from numerical simulation at (a) $t = 6000$ s, (b) $t = 7200$ s and (c) $t = 8000$ s. All dimensions are in m.

to the eutectic composition. With shift in concentration of the bulk fluid towards the eutectic composition, the temperature difference between the solidus and liquidus also keeps decreasing, leading to a thinning of the mushy layer. After about 25 000 s from the start of the experiment, the liquid composition reaches the eutectic state, causing the mushy layer to vanish. Thereafter, there is no further change in bulk liquid composition, and the mixture solidifies isothermally. Hence, even though the convection strength decreases with further progress in solidification (due to a thinning of the liquid layer height), it does not cause any reappearance or thickening of the mushy layer.

As mentioned earlier, during the experimental investigation, temperatures have been monitored using a set of thermocouples. The experimental temperature–time history is compared with the corresponding numerical simulations using the measured top and bottom wall temperatures as boundary conditions. A typical temperature–time history is shown in Fig. 15, corresponding to a thermocouple location at a height of 28.5 mm from the bottom, located on the central vertical axis of the cavity. It is observed that the cooling rate is quite fast in the beginning, owing to an imposed cooling at the top boundary. However, the temperature curve starts flattening after some time (at $t \approx 10\,000$ s), and stabilizes to a nearly constant value at a later stage during solidification. We may observe here that this trend of temperature variation with time is similar to that of the top wall shown in Fig. 3. The flattening of the temperature–time curve corresponds to the initiation of solidification at the top surface. The latent heat release during solidification decreases the cooling rate of the top surface, and thereby stabilizes the top wall temperature. The turbulent convection ensures good mixing in the liquid layer, thus causing an interior point (such as the thermocouple location) in the liquid to experience a temperature–time trend similar to that of the top wall. Temperature–time history at other vertical positions are also recorded (not shown here), and a similar behaviour is observed. Interestingly, the flattening of the cooling curves seem to occur approximately at the same time in

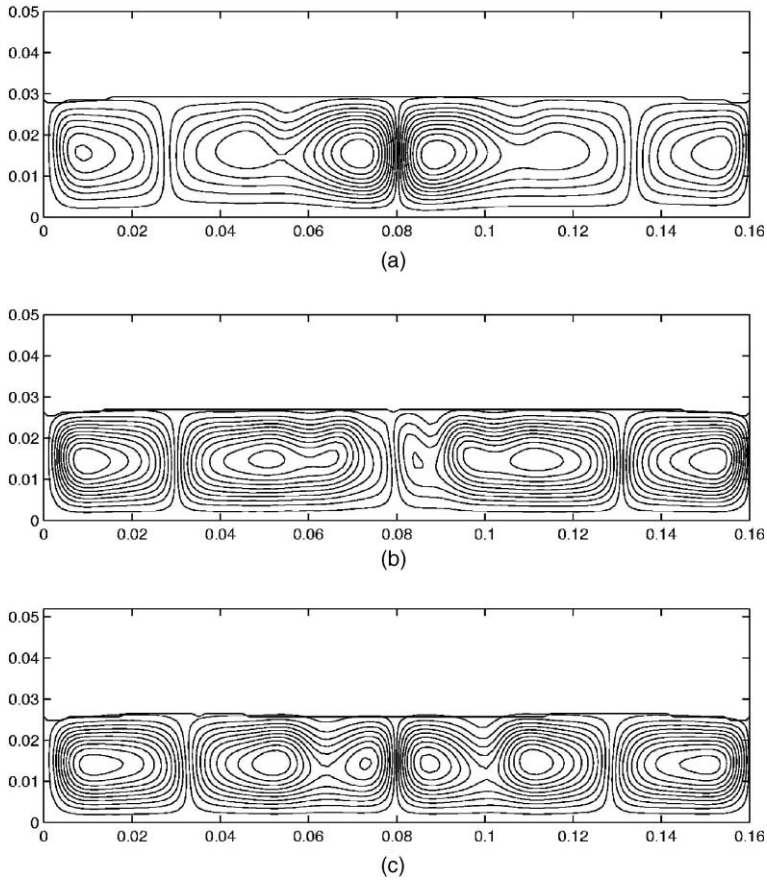

Fig. 7. Evolution of flow with time, as obtained from numerical simulation at (a) $t = 8800$ s, (b) $t = 9800$ s and (c) $t = 10900$ s. All dimensions are in m.

each case, irrespective of the thermocouple location. Corresponding numerical simulations show a good agreement with the experimental plots in all the above cases.

A general interaction between heat transfer, mass transfer and fluid flow during the evolution of the solidification process can be better understood by studying the variation of Rayleigh number (based on instantaneous liquid layer height) with time, as depicted in Fig. 16. It can be observed from the above figure that the thermal Rayleigh number (Ra_T) is maximum at the beginning of the solidification process, primarily because of the maximum liquid layer height present initially. Once the interface starts advancing towards the bottom of the cavity, the effective liquid layer height progressively goes down, leading to a continuous decrease of the thermal Rayleigh number. In addition, the temperature difference between the bottom boundary and the solidification interface decreases asymptotically, thus enhancing the decrease of the thermal Rayleigh number. The solutal Rayleigh number (Ra_S), on the other hand, is influenced by two opposing effects. A continuous thinning of the liquid layer has a tendency to lower the solutal Rayleigh number. At the same time, a continuous solute rejection with progress in solidification enhances the concentration gradients acting across the domain, thus tending to increase the solutal Rayleigh number. The resultant variation in Ra_S, therefore, depends on the relative strengths of these two opposing factors. However, once the solute concentration in the liquid (C_l) reaches eutectic concentration (C_E), the concentration difference ($C_l - C_i$) becomes a constant. A further decrease in liquid layer height, therefore, results in a monotonic decrease in the solutal Rayleigh number. The resultant Rayleigh number ($Ra = Ra_T + Ra_S$) initially follows the trend represented by the thermal Rayleigh number, since thermal gradients are much stronger than solutal gradients at early stages of solidification. A solidification progresses, thermal Rayleigh number becomes relatively insignificant in comparison to the solutal Rayleigh number, at about $t = 1.5 \times 10^4$ s (Fig. 16). Thereafter the resultant Rayleigh number

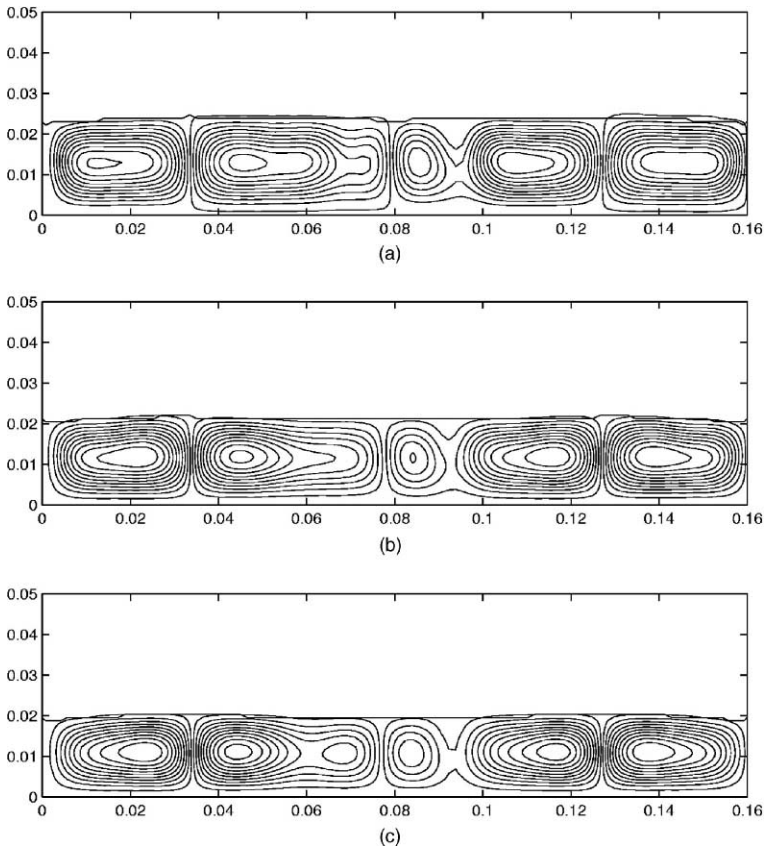

Fig. 8. Evolution of flow with time, as obtained from numerical simulation at (a) $t = 12100$ s, (b) $t = 13200$ s and (c) $t = 15000$ s. All dimensions are in m.

follows closely the trend presented by the solutal Rayleigh number at later stages of solidification.

Fig. 17 represents the variation of Nusselt number (Nu) with Rayleigh number (Ra) during the entire process. It can be noted here that the above Nusselt number is based on the heat flux at the interface, i.e. $(Nu = (q''_{\mathrm{liq}} h_{\mathrm{l}})/(k_{\mathrm{T},L}(T_{\mathrm{h}} - T_{\mathrm{c}}))$. It can be observed from Fig. 17(a) that as the effective Rayleigh number decreases, the Nusselt number also decreases. The variation of Nusselt number is not linear, but can be closely approximated as a power law variation, with the exponent approximately equal to 0.3. This trend matches well with some other familiar instances of turbulent Benard convection. However, to have a closer look at the variation of Nusselt number at lower ranges of Rayleigh number, the curve in Fig. 17(a) is zoomed in Fig. 17(b), within a Rayleigh number range $0–2 \times 10^4$. It can be clearly observed that there is an abrupt change in slope of the curve at a Rayleigh number of about 2×10^3. This, in effect, represents the critical Rayleigh number, below which fluid motion completely dies down, and heat transfer takes place only by conduction. Below this Rayleigh number, the Nusselt number comes out to be unity, which suggests that advection effects are not present once the Rayleigh number becomes less than this critical value.

6. Conclusions

A modified k–ε model for numerical simulation of turbulent transport during non-equilibrium solidification processes of binary alloys is presented. By invoking appropriate constitutive relations representing species transport at the microscopic level, metallurgically consistent predictions from the present model are effectively ensured. Particular emphasis is given for appropriate modeling of turbulence parameters, so that the model merges with single-phase turbulence closure equations in the pure liquid region in a smooth manner. Laboratory experiments are performed using an NH_4Cl–H_2O solution kept in a rectangular cavity that is solidified by cooling from the top. Cellular flow patterns below the continuously deforming solidification interface are observed, as the flow transits from turbulent to the laminar regime. Growth rates of mushy and solid interfaces are

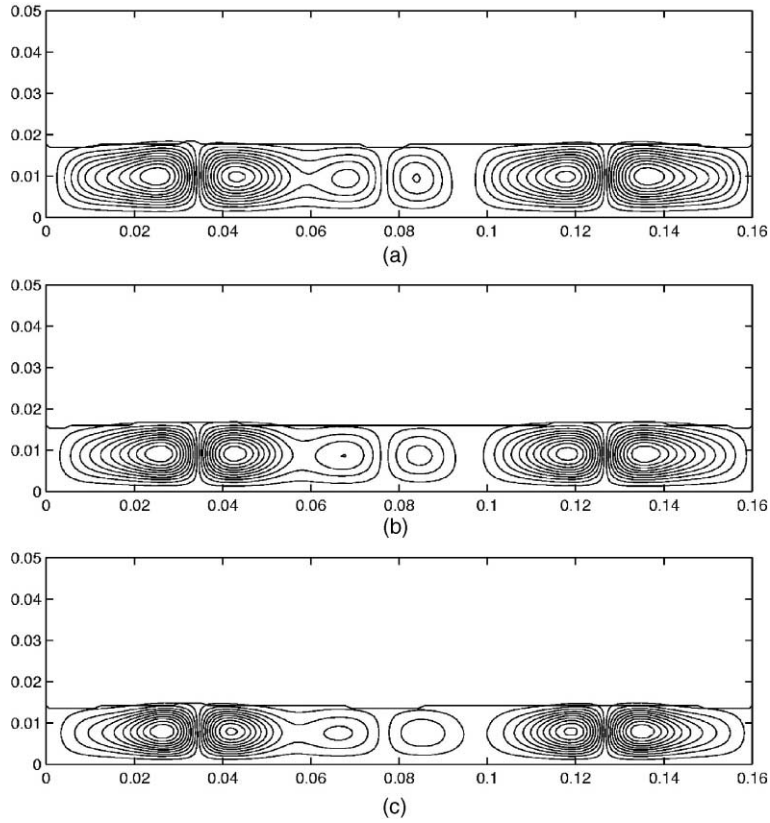

Fig. 9. Evolution of flow with time, as obtained from numerical simulation at (a) $t = 16000$ s, (b) $t = 17500$ s and (c) $t = 21800$ s. All dimensions are in m.

also measured, and are compared with corresponding numerical predictions. In addition, thermal evolution recorded during experiments are compared with corresponding numerical results. For all cases, a good agreement between numerical and experimental results can be observed. Finally, a variation of some important non-dimensional convection parameters such as the Rayleigh number and Nusselt number is obtained, depicting a clear picture of interaction between turbulent Rayleigh–Benard convection and directional solidification.

Appendix A. Discretization of convective and diffusive flux

In the present control volume approach, the fluid flow equations are solved using the SIMPLER algorithm [15]. For the other conservation equations (such as the energy and species conservation equations, as well as the governing equations for turbulent kinetic energy and dissipation rate of turbulent kinetic energy), the convection–diffusion fluxes are discretized using a power-law scheme [15]. However, there are additional advective fluxes on account of evolution of latent heat during the solidification process, which are discretized using an 'upwind' scheme. Integration of the above advective fluxes over a control volume yields:

$$\int_{CV} \nabla(\rho \vec{u} \Delta H)\,\mathrm{d}V = \text{flowout} - \text{flowin}$$

where

$$\begin{aligned}\text{flowin} = {} & \Delta H_W \max(F_w, 0) - \Delta H_P \max(-F_w, 0) \\ & + \Delta H_S \max(F_s, 0) - \Delta H_P \max(-F_s, 0),\end{aligned}$$

and

$$\begin{aligned}\text{flowout} = {} & \Delta H_P \max(F_e, 0) - \Delta H_E \max(-F_e, 0) \\ & + \Delta H_P \max(F_n, 0) - \Delta H_N \max(-F_n, 0) \quad \text{(A.1)}\end{aligned}$$

It can be noted that subscripts e, w, s, n, E, W, S, N in Eq. (A.1) are in accordance with the usual nomenclature of control points in the context of description of a control volume in finite volume procedure, as sketched in figure (A.1). 'F' in Eq. (A.1) denotes the mass flow rate across the respective face of the control volume.

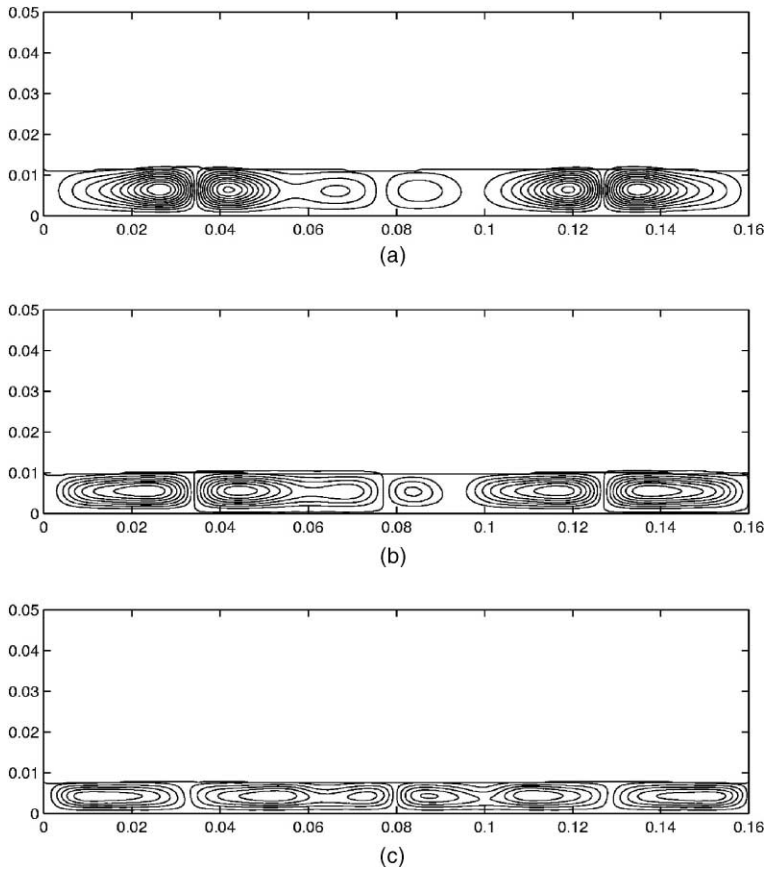

Fig. 10. Evolution of flow with time, as obtained from numerical simulation at (a) $t = 29000$ s, (b) $t = 33500$ s and (c) $t = 35500$ s. All dimensions are in m.

Appendix B. Generalized enthalpy updating scheme

For accurate prediction of the of the liquid fraction in the present 'fixed-grid enthalpy-based' procedure, the latent heat content of each computational cell needs to be updated according to the temperatures predicted by the macroscopic conservation equations, during each iteration within a time-step. In a physical sense, such updating attempts to neutralize the difference in the nodal temperatures predicted by the energy equation, and that dictated by the phase-change considerations. In the present context, we choose an iterative update scheme proposed by Brent et al. [20], which is of the form:

$$[\Delta H_P]_{n+1} = [\Delta H_P]_n + \frac{a_P}{a_P^0}\lambda\left[\{h_P\}_n - F^{-1}\{\Delta H_P\}_n\right] \qquad \text{(B.1)}$$

where $a_P^0 = \rho\Delta V/\Delta t$, a_P is the coefficient of T_P in the discretization equation of the governing energy equation [15], λ is a relaxation factor, and F^{-1} is a suitable function depending on the phase change morphology. Here, ΔV is the volume of a computational cell centred around the grid pint P, Δt is the time-step chosen and h_P is the sensible enthalpy appropriate to the nodal point P. The physical meaning of the term a_P/a_P^0 is described in Brent et al. [20]. It may be noted here that although the paper by Brent et al. [20] essentially deals with pure metals, the formulation of enthalpy update can be extended to alloy solidification problems with a proper choice of F^{-1} function. Hence, F^{-1} needs to be devised for the alloy solidification problem consistently with the microscopic physics followed in the mathematical formulation, so that physically meaningful results pertaining to a specific solidification model can be obtained. Guidelines to the choice of appropriate form of the function F^{-1} are presented in Chakraborty and Dutta [21]. In the subsequent discussion, the procedure is outlined in brief, which is suitable for most metallurgical phase change situations. The aim is to prepare a guideline so that metallurgically inconsistent results from a macroscopic model can be avoided.

As a starting point, the metallurgical phase diagram in a general functional form of $T = T(T_L, T_m, \frac{C_0}{C_l})$ can be

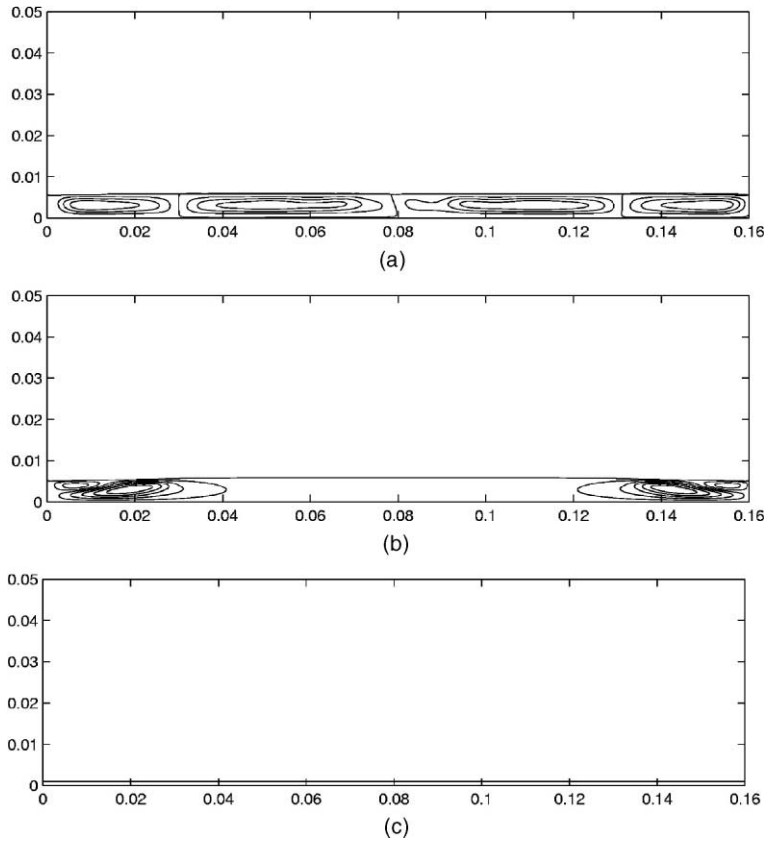

Fig. 11. Evolution of flow with time, as obtained from numerical simulation at (a) $t = 37\,500$ s, (b) $t = 39\,500$ s and (c) $t = 42\,000$ s. All dimensions are in m.

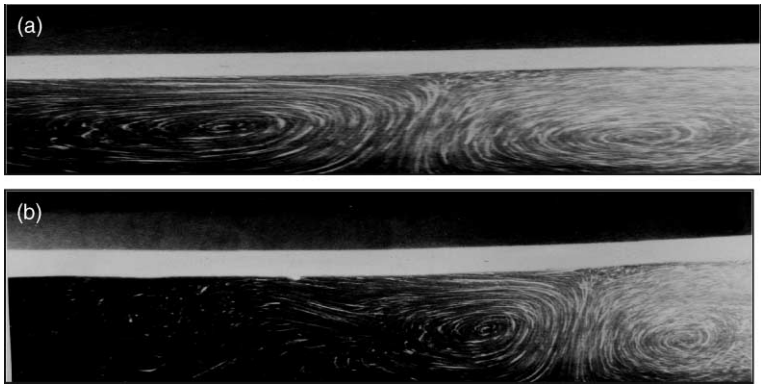

Fig. 12. Photographs of experimental flow visualization (a) zoomed in the middle portion of the cavity, resembling a corresponding numerical simulation shown in Fig. 7a, (b) zoomed near the right corner of the cavity, resembling a corresponding numerical simulation shown in Fig. 7b.

considered, where T_L, T_m, C_0, and C_l are the liquidus temperature, melting temperature (of a pure component), nominal alloy concentration, and liquid composition, respectively. As a specific example, this function may take the following form:

$$T = T_L \frac{C_l}{C_0} - T_m \left(\frac{C_l}{C_0} - 1 \right), \tag{B.2}$$

for the case of a linearized phase diagram, which is a common assumption in many of the macroscopic mod-

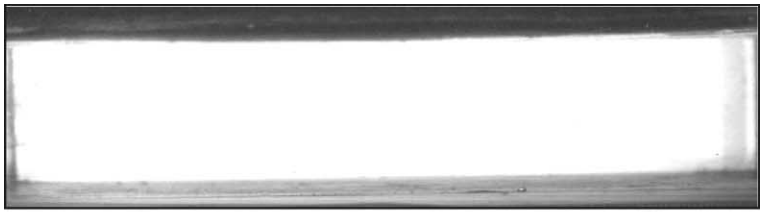

(a) t = 2400s

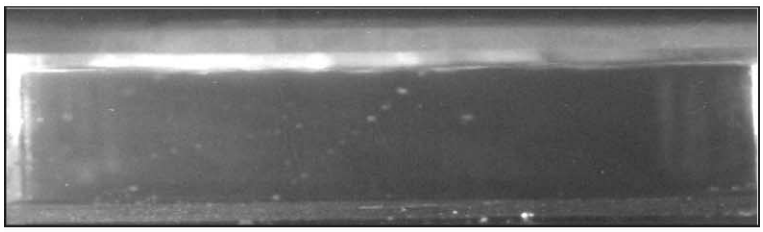

(b) t = 6180s

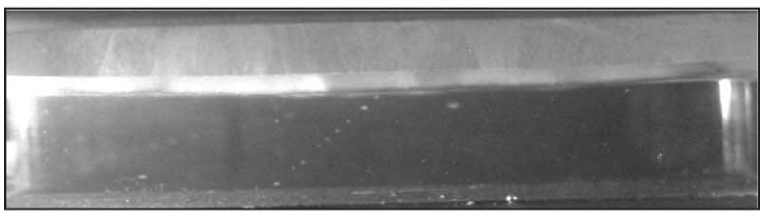

(c) t = 8820s

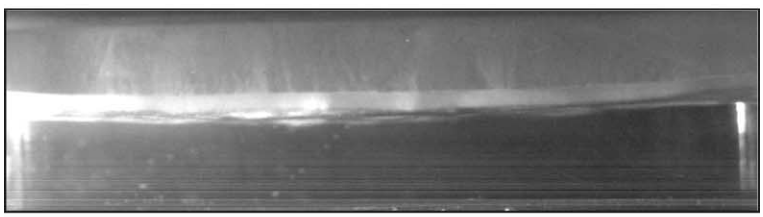

(d) t = 10800s

(e) t = 27780s

Fig. 13. A visualiszation of the evolution of interface (experimental).

els quoted in the literature [12]. The next step is to substitute the proper metallurgical relation for C_0/C_l as a function of liquid fraction (depending upon the metallurgical model under consideration), appropriately representing the microscopic solute balance. For the case of a non-equilibrium solidification situation, the above may be described by Scheil's model [12] as:

$$(C_l - C_s)\mathrm{d}f_s = (1 - f_s)\mathrm{d}C_l, \tag{B.3}$$

where f_s is the mass fraction of the solid, and C_s is the solid phase composition. On integrating Eq. (B.3), one obtains

$$f_l = \exp\left\{ -\int_{C_0}^{C_l} \frac{\mathrm{d}C_l}{C_l(1 - k_p)} \right\} \tag{B.4}$$

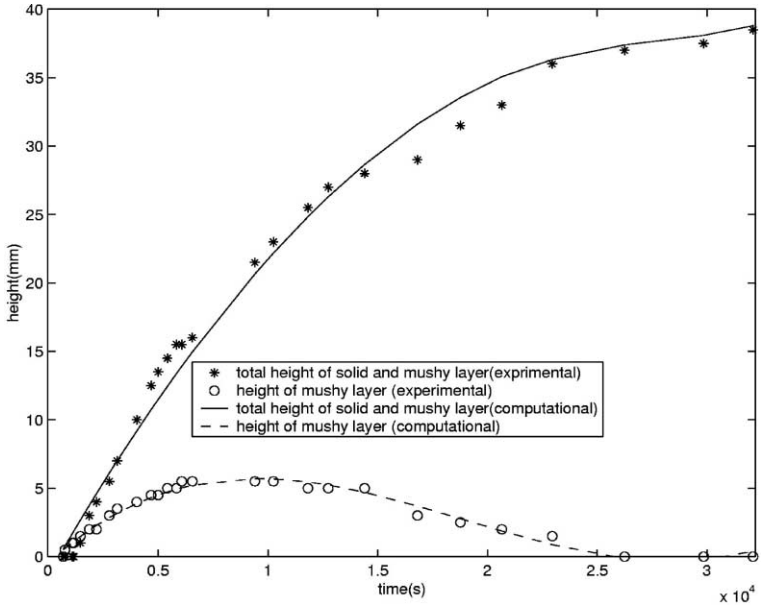

Fig. 14. Evolution of the visualization experiment along with the height of the solidified layer.

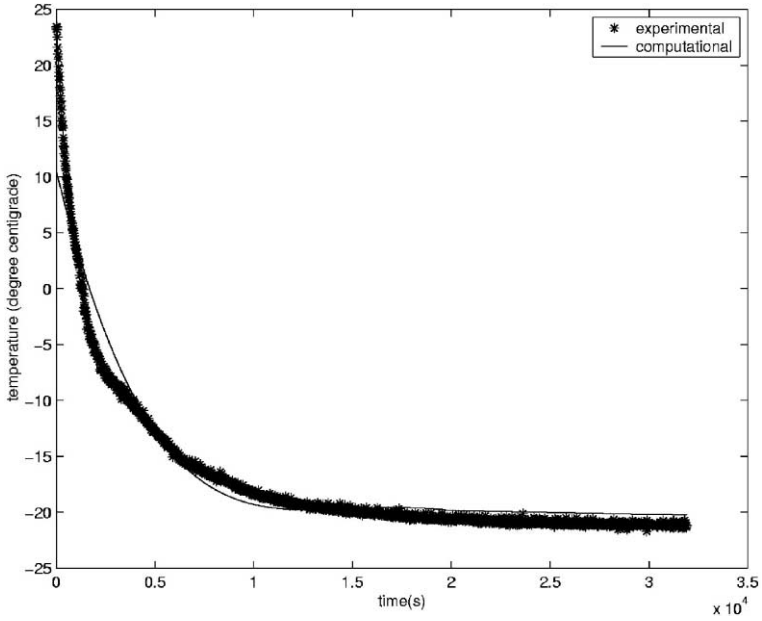

Fig. 15. Evolution of temperature with time, as obtained experimentally and numerically, corresponding to a thermocouple located at a distance 28.5 mm vertically upwards from the bottom wall, along the centerline of the cavity.

where f_l is the mass fraction of the liquid, and k_p is the partition-coefficient. Eq. (B.4), in principle, can be integrated if the variation of k_p with C_l is known. For the specific case of a constant partition-coefficient (or, a partition-coefficient independent of composition), integration of Eq. (B.4) gives:

$$C_l = C_0 f_l^{k_p - 1} \tag{B.5}$$

Now, substituting Eq. (B.4) in Eq. (B.1), and using $f_l = \Delta H/L$, one obtains

$$\frac{h - cT_L}{h - cT_m} = 1 - \left(\frac{\Delta H}{L}\right)^{(1-k_p)} \tag{B.6}$$

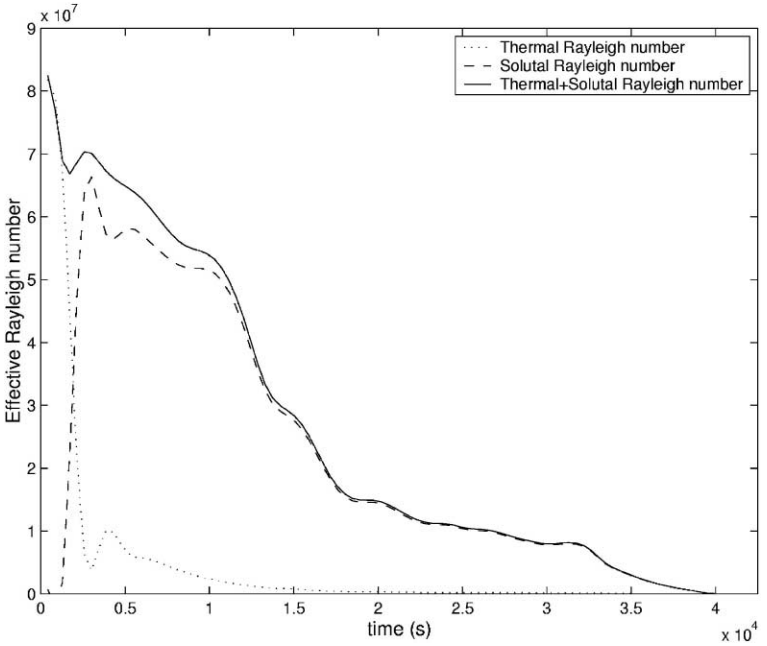

Fig. 16. Variation of Rayleigh number with time.

From Eq. (B.6) one gets

$$F^{-1}(\Delta H) = T_{\mathrm{m}} - (T_{\mathrm{m}} - T_{\mathrm{L}})\left(\frac{\Delta H}{\mathrm{L}}\right)^{(k_{\mathrm{p}}-1)}. \tag{B.7}$$

Eq. (B.7) is an expression for the inverse of the latent heat function corresponding to the case of non-equilibrium solidification described by Scheil's model. It has to be noted that T_{L} in the above equations is not a constant, but a natural variable occurring during the phase-change process, which can be determined from the current value (during iteration) of the nominal alloy composition using the phase-diagram information.

From the above illustration, the summary of the basic steps to obtain metallurgically consistent latent heat functions for numerical simulation of any solidification process can be outlined. It can be noted that, an essential pre-requisite is first to identify the governing metallurgical relation for solidification, physically consistent with the model under consideration (namely lever rule, Scheil's equation, Brody–Flemings equation etc.). Then, for each iteration, the following steps are to be sequentially followed:

Step 1: Obtain the temperature-concentration coupling from the phase diagram in a functional form.

Step 2: Calculate T_{L} and T_{S} corresponding to the current iteration value of the nominal alloy composition, using step 1.

Step 3: Substitute the metallurgical governing relation for concentration in terms of liquid fraction (for example, Scheil's equation), in the functional form of step 1.

Step 4: Write f_{l} as $\Delta H/L$ and T as, h/c in the algebraic form obtained from step 1.

Step 5: Solve from step 4, to find an expression for F^{-1} explicitly.

Step 6: Constrain the F^{-1} thus formed in meaningful limits, i.e., if $F^{-1} > T_{\mathrm{L}}$, $F^{-1} = T_{\mathrm{L}}$; if $F^{-1} < T_{\mathrm{S}}$, $F^{-1} = T_{\mathrm{S}}$.

It can be noted that the above outline is fairly general, and can be applied to several metallurgical models governing the phase-change behaviour.

Appendix C. Updating of C_μ

The liquid fraction at any control volume it can be found out as $f_{\mathrm{l}} = (\Delta H/L)$, once the latent heat updating is performed. Thereafter, C_μ is updated as:

$$C_\mu^n = \sqrt{f_{\mathrm{l}}^n}\exp\left(-\frac{3.4}{\left[1+\frac{\rho(k^{n-1})^2}{50\mu\varepsilon^{n-1}}\right]^2}\right) \tag{C.1}$$

where C_μ^n is the value of C_μ in a control volume for the nth iteration, f_{l}^n is the liquid fraction in a control volume for

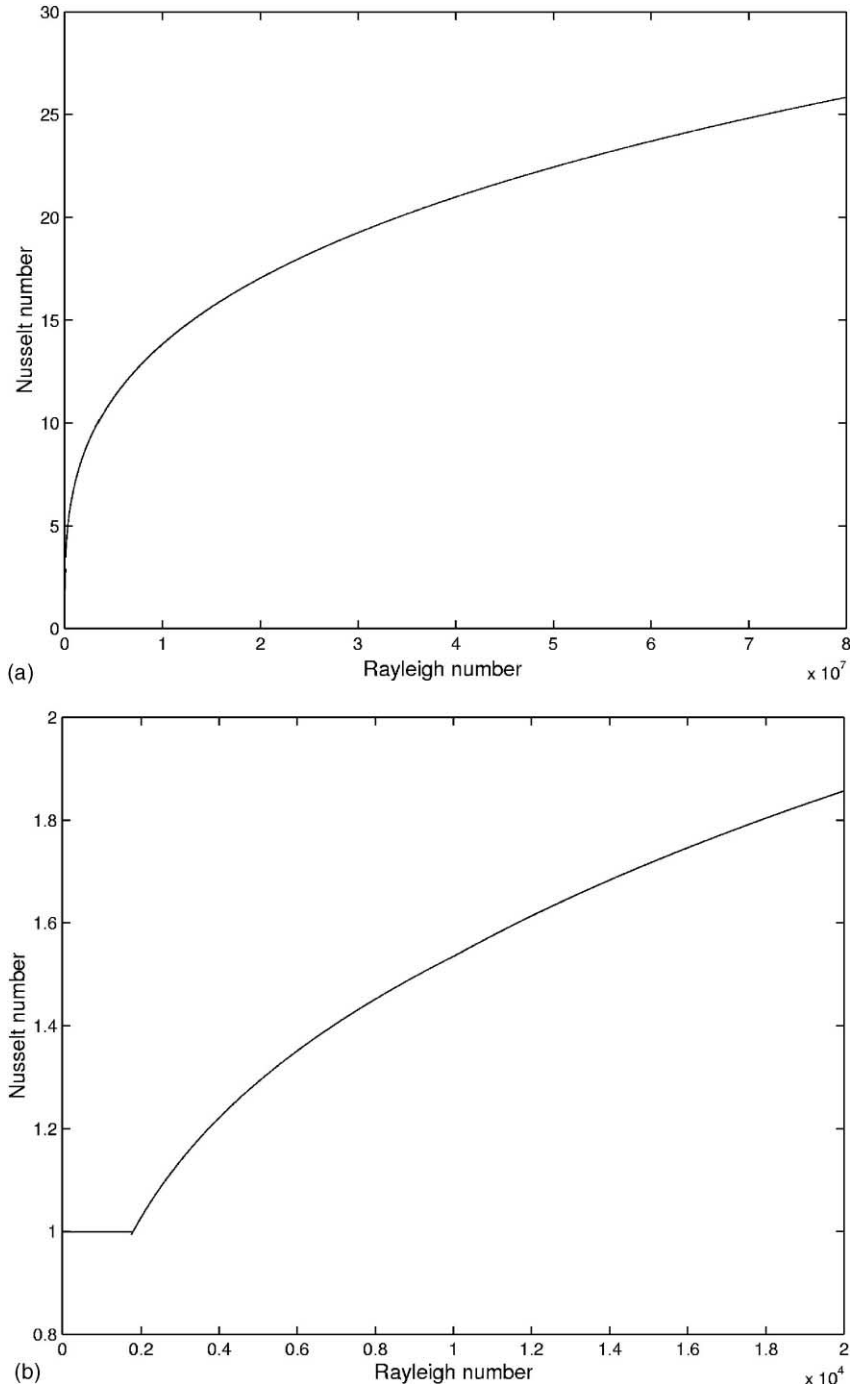

Fig. 17. Variation of Nusselt number (based on heat flux at the liquidus interface) with Rayleigh number (a) over the entire range of variation of Rayleigh number and (b) in a small range of Rayleigh number depicting flow characteristics towards the end of solidification.

nth iteration, k^{n-1} is the value of turbulent kinetic energy at $(n-1)$th iteration at the corresponding point, and ε^{n-1} is the value of dissipation rate of turbulent kinetic energy at $(n-1)$th iteration at the grid point of concern.

Accordingly, the value of eddy viscosity, μ_t^n, at that point for nth iteration is given by:

$$\mu_t^n = \rho C_\mu^n \frac{(k^{n-1})^2}{\varepsilon^{n-1}} \tag{C.2}$$

References

[1] H.E. Huppert, The fluid mechanics of solidification, J. Fluid Mech. 212 (1990) 209–240.

[2] R.C. Kerr, A.W. Woods, M.G. Worster, H.E. Huppert, Solidification of an alloy cooled from above. Part I: Equilibrium model, J. Fluid Mech. 216 (1990) 323–342.

[3] R.C. Kerr, A.W. Woods, M.G. Worster, H.E. Huppert, Solidification of an alloy cooled from above. Part 2: Non-equilibrium interfacial kinetics, J. Fluid Mech. 217 (1990) 331–348.

[4] R.C. Kerr, A.W. Woods, M.G. Worster, H.E. Huppert, Solidification of an alloy cooled from above Part 3: Compositional stratification within the solid, J. Fluid Mech. 218 (1990) 337–354.

[5] W. Shyy, Y. Pang, D.Y. Wei, M.H. Chen, Effects of surface tension and buoyancy on continuous ingot solidification, AIAA 28th Aerospace Science Meeting, Paper number 91-0506, 1991.

[6] W. Shyy, Y. Pang, G.B. Hunter, D.Y. Wei, M.H. Chen, Modeling of turbulent transport and solidification during continuous ingot casting, Int. J. Heat Mass Transfer 35 (1992) 229–1245.

[7] M.R. Aboutealebi, M. Hasan, R.I.L. Guthrie, Coupled turblent flow, heat and solute transport in continuous casting processes, Metallurg. Mater. Trans. 26B (1995) 731–744.

[8] S.H. Seyedein, Three-dimensional modeling of various slab and thin-strip twin roll casting processes, Ph.D. Thesis, McGill University, Department of Mining and Metallurgical Engineering, 1997.

[9] R.P. Tavares, Vertical twin-roll caster: metal-mould heat transfer, solidification and product characterization, Ph.D. Thesis, McGill University, Department of Mining and Metallurgical Engineering, 1997.

[10] P.G.Q. Netto, R.I.L. Guthrie, Int. J. Heat Mass Transfer 43 (2000) 21–37.

[11] W.D. Bennon, F.P. Incropera, A continuum model for momentum, heat and species transport in binary solid-liquid phase change system—I. Model formulation, Int. J. Heat Mass Transfer 30 (1987) 2161–2170.

[12] V.R. Voller, A.D. Brent, C. Prakash, The modeling of heat, mass and solute transport in solidification systems, Int. J. Heat Mass Transfer 32 (1989) 1719–1731.

[13] M.C. Flemings, Solidification processing, McGraw Hill, New York, 1974.

[14] P.J. Prescott, F.P. Incropera, W.D. Bennon, Modeling of dendritic solidification systems: reassessment of the continuum momentum equation, Int. J. Heat Mass Transfer 34 (1991) 2351–2358.

[15] S.V. Patankar, Numerical heat transfer and fluid flow, Hemisphere, Washington, DC, 1980.

[16] D. Morvan, M. El Ganaoui, P. Bontoux, Numerical simulation of a crystal growth problem in vertical Bridgman-Stockbarger furnace: Latent heat effect and crystal-melt interface morphology, Int. J. Heat Mass Transfer 42 (1999) 573–579.

[17] T. Masuoka, Y. Takatsu, Turbulence model for flow through porous media, Int. J. Heat Mass Transfer 39 (1996) 2803–2809.

[18] T. Komatsu, N. Matsunaga, 1986. Defect of k–ε Turbulence Model and its Improvements, Proc. 30th Japan Conference on Hydraulics, pp. 529–534.

[19] P. Kumar, S. Chakraborty, K. Srinivasan, P. Dutta, Studies on Transport Phenomena during Directional Solidification of a Binary Alloy Solution Cooled from the Top (communicated), 2001.

[20] A.D. Brent, V.R. Voller, K.J. Reid, The enthalpy porosity technique for modelling convection–diffusion phase change: application to the melting of a pure metal, Numer. Heat Transfer 13 (1988) 297–318.

[21] S. Chakraborty, P. Dutta, A generalized formulation for evaluation of latent heat functions in enthalpy-based macroscopic models for convection–diffusion phase change processes, Metallurg. Mater. Trans. B 32B (2001) 562–564.